de Haas–van Alphen Effect in Mercury*

G. B. Brandt† and J. A. Rayne

Carnegie Institute of Technology, Pittsburgh, Pennsylvania

(Received 11 March 1966)

By means of de Haas–van Alphen studies on oriented single crystals, the topology and size of the Fermi surface of mercury have been determined. Three distinct types of oscillations with minimum values of $f(1/H)$ equal to 7.35×10^5, 1.58×10^7, and 3.22×10^7 G have been observed in the field range 10 to 60 kG. The data are discussed in terms of both the free-electron model and a three-parameter plane-wave model. Only one set of oscillations corresponds to features of the former, namely, lens-shaped second-zone electron surfaces on {100} faces of the Brillouin zone. The plane-wave model with pseudopotential parameters V_{100}, V_{110}, and V_{111} equal to -0.066, $+0.047$, and $+0.047$ Ry, respectively, produces the modification of the free-electron first-zone hole surface necessary to explain the existence of the other oscillations.

I. INTRODUCTION

MERCURY has interested metal physicists for many years because it is purified easily by distillation. However, little knowledge has been obtained of its electronic band structure as a solid, because of the difficulty in handling and orienting the soft single crystals at temperatures well below their melting point ($-38.8°C$). Verkin, Lazerev, and Rudenko[1] and Schoenberg[2] independently discovered the existence of the de Haas–van Alphen (dHvA) effect in samples of mercury grown *in situ* within the experimental apparatus. Shoenberg, whose work was the more extensive of the two, observed large dHvA oscillations in samples whose orientations were determined from their magnetic anisotropy. These oscillations, of minimum frequency $f(1/H)=7.2\times10^5$ G, were associated with small, highly anisotropic portions of the Fermi surface. The complexity of their behavior indicated that further progress in understanding the Fermi surface of mercury would require accurate knowledge of the sample orientation.

This work reports the results of dHvA measurements on single crystals of mercury accurately oriented by conventional x-ray means. Data were obtained using two techniques, the torque-balance method[3] and the rf method,[4] over the magnetic-field range from 10 to 60 kG. The topology and size of the Fermi surface have been determined from the data and a three-parameter plane-wave model has been constructed, which reproduces in essential details the observed features of the Fermi surface.

[1] B. I. Verkin, B. G. Lazarev, and N. S. Rudenko, Dokl. Akad. Nauk SSSR **80**, 45 (1951).

[2] D. Shoenberg, Phil. Trans. **A245**, 1 (1952).

[3] J. H. Condon and J. A. Marcus, Phys. Rev. **134**, A446 (1964).

[4] D. Shoenberg and P. J. Stiles, Proc. Roy. Soc. (London) **281A**, 62 (1964).

II. THEORY

a. de Haas–van Alphen Effect

Since the de Haas–van Alphen effect is now a well-established tool for the determination of the band structure of metals, its theoretical derivation will not be considered here. The usual arguments show that for a metal the free energy F and its derivatives, the moment $M=-\partial F/\partial H$ and the torque $C=-\partial F/\partial\theta$, are periodic in harmonics of the inverse magnetic field $1/H$. The fundamental frequency $f(1/H)$ of these oscillations is related to an extremal cross-sectional area of the Fermi surface (FS) by the equation[5]

$$A_{\text{extremal}}=(2\pi e/c\hbar)f(1/H),\qquad(1)$$

or equivalently

$$A_{\text{extremal}}(\text{Å}^{-2})=9.55\times10^{-9}f(1/H).\qquad(2)$$

It is readily demonstrated[6] that the expression for the oscillatory component of the torque involves the factor $dA/d\theta$. This factor vanishes for isotropic Fermi surfaces in all field directions, as well as for anisotropic surfaces with the field oriented along symmetry directions. Thus measurements of the oscillatory susceptibility by the torque method are not always possible. Nevertheless when it is feasible, this technique is very useful in measuring very low-frequency oscillations, corresponding to small sections of the Fermi surface.

The dHvA oscillations in the magnetic susceptibility can be detected also by observing their effect on the coupling between two coils wound concentrically about the sample, one a modulating coil driven at a fundamental frequency, and the other a pickup coil connected to a suitable receiver. When the sample susceptibility is a nonlinear function of the field, the signal at the receiver consists of the fundamental as well as the its second and higher harmonics. All of these components, which arise from the magnetization M and its derivatives with respect to the magnetic field, oscillate with the

[5] L. Onsager, Phil. Mag. **43**, 1006 (1952).

[6] D. Shoenberg, in *Progress in Low Temperature Physics II*, edited by C. J. Gorter (Interscience Publishers, Inc., New York, 1957), pp. 226 ff.

TABLE I. Crystallographic data for Hg.

Symbol	Value	Value (units of b_0)	Definition
a_0	2.9863 Å	$\cdots$	Rhombohedral vector at 5°K[a]
α	70°44.6′	$\cdots$	Rhombohedral angle at 5°K[a]
b_0	1.0932($2\pi/a_0$) ($=2.3002$ Å^{-1})	1.0000	Reciprocal lattice vector[a]
β	104.36°	$\cdots$	Rhombohedral angle for reciprocal lattice
θ'	65.80°	$\cdots$	Angle between (100), b_0, and trigonal axis, (111)
ϕ'	48.05°	$\cdots$	Angle between (110) and (111)
V	$0.8631a_0{}^3$ ($=22.986$ Å^3)	$\cdots$	Volume of unit cell
$2\pi/a_0$	2.1040 Å^{-1}	$\cdots$	
$\Gamma\text{-}L$	1.1500 Å^{-1}	0.5000	$\frac{1}{2}$(100)
$\Gamma\text{-}X$	1.4103 Å^{-1}	0.6131	$\frac{1}{2}$(110)
$\Gamma\text{-}T$	1.4144 Å^{-1}	0.6149	$\frac{1}{2}$(111)
k_F	1.3708 Å^{-1}	0.5960	Fermi radius
E_F	0.5240 Ry	0.355[b]	Fermi energy
$X\text{-}U$	$\cdots$	0.2363	$\frac{1}{2}$ length of (110) face of Brillouin zone
$T\text{-}U$	$\cdots$	0.2719	$\frac{1}{2}$ width of (111) face of Brillouin zone
$L\text{-}U$	$\cdots$	0.4494	
$\begin{cases}X\text{-}K\\U\text{-}W\end{cases}$	$\cdots$	0.1570	$\frac{1}{2}$ width of (110) face of Brillouin zone
$T\text{-}W$	$\cdots$	0.3139	

[a] Magnitudes of these vectors in italics.
[b] Units of $\hbar^2 b_0{}^2/2m$.

dHvA frequency $f(1/H)$. Although the higher harmonics are of smaller amplitude than the fundamental, they are not superimposed on the large nonoscillating signal produced by the monotonic increase of M with H and the magnetoresistance.

Shoenberg and Stiles[4] have computed the expression for the amplitude of the second-harmonic voltage in the frequency limit of strong skin effect. Their result for the voltage V induced in a coil of N turns and radius a for a modulating field of magnitude h_0 is

$$V = 2\pi a N\left[(1+4\pi dM/dH)\frac{\omega}{4\pi\sigma}\right]^{1/2}\left(h_0\cos(\omega t+\tfrac{1}{4}\pi)\right.$$
$$\left.+\left[\frac{4\pi d^2 M/dH^2}{1+4\pi dM/dH}\right]\frac{h_0{}^2}{4}(2-\sqrt{2})\cos(2\omega t+\tfrac{1}{4}\pi)\right). \quad (3)$$

In Eq. (3) ω and σ have their usual meanings of frequency and conductivity, while dM/dH and d^2M/dH^2 are the derivatives of the magnetization with respect to field. Because this calculation was carried out only to second order, the third and higher harmonics do not appear. The ratio of the second-harmonic amplitude to that part of the fundamental proportional to dM/dH (and hence that part which will vary with dHvA oscillations) is given by

$$\frac{V_{2\omega}}{V_\omega} = \frac{h_0}{4}(2-\sqrt{2})\frac{d^2M/dH^2}{dM/dH}$$
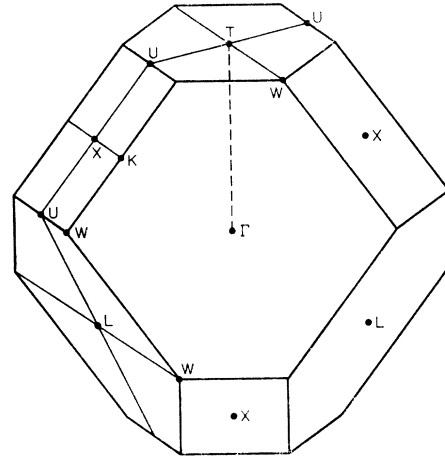$$= \frac{\pi}{2}(2-\sqrt{2})\frac{h_0}{\Delta H} \approx \frac{h_0 f(1/H)}{H^2}, \quad (4)$$

FIG. 1. The Brillouin zone of mercury with the symmetry points labeled according to the notation of Cohen (Ref. 8). The zone center is Γ and the plane of projection is perpendicular to $\Gamma\text{-}L$, a (100) reciprocal lattice vector.

where ΔH is the field interval between two dHvA maxima and $f(1/H)$ is the dHvA frequency in $1/H$. From this equation it is clear that the magnitude of the second-harmonic component can be made equal to that of the varying fundamental component, providing that modulation fields of the magnitude of the dHvA field interval are used. Furthermore, since the magnitude of the second harmonic relative to the fundamental is proportional to the dHvA frequency, this method will be sensitive to high dHvA frequencies (large areas of FS) in preference to low ones (small areas). Unlike the torque method, the field-modulation technique is still applicable along symmetry directions.

In the limit that $2\pi^2\kappa T/\beta^* H\gg 1$ ($\beta^*=e\hbar/m^* c$, i.e., the double effective Bohr magneton), the temperature dependence of the dHvA oscillations is given essentially by $\exp(-2\pi^2\kappa T/\beta^* H)$. The effective mass of the associated carriers can thus be determined from the slope at a plot of $\ln C/T$ versus T or $\ln V_{2\omega}/T$ versus T.[2,4] In both cases the slope is equal to

$$S = -2\pi^2\kappa/\beta^* H, \quad (5)$$

implying that

$$m^*/m_0 = -S\beta_0 H/\pi^2\kappa, \quad (6)$$

where β_0 is the Bohr magneton.

b. Free-Electron Fermi Surface for Mercury

In order to clarify the interpretation of the dHvA-effect data it is helpful to keep in mind some sort of model for the Fermi surface. The free-electron model for mercury is described here not because it is an accurate representation of the actual FS, but because it is an easily constructed and simply visualized approximation. The free-electron model exhibits the full symmetry of the lattice and hence the symmetry of whatever results are produced by a more elaborate calcula-
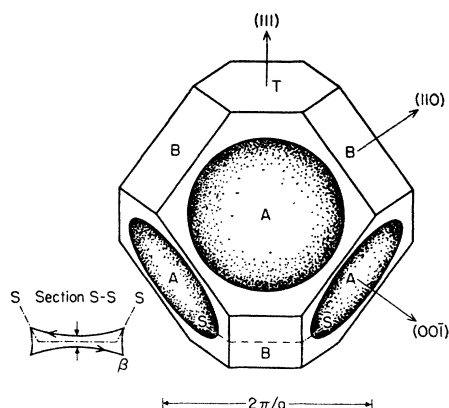
Fig. 2. The first-zone hole surface for mercury according to the free-electron model. The inscribed sphere does not touch either the T or B faces of the Brillouin zone.

tion. Furthermore, for the portions of the Fermi surface resulting from the lower bands in the crystal, the actual FS should be a recognizable distortion of the free-electron case.

The crystal structure of mercury is rhombohedral with lattice constant 2.9963 Å and rhombohedral angle α of 70°44.6' as measured by Barrett[7] at 5°K. This structure may be considered a distorted version of the more common face-centered-cubic structure, for which the appropriate angle is 60 deg. The reciprocal lattice for mercury is also rhombohedral, with rhombohedral angle β given in Table I. Figure 1 shows the Brillouin zone for the structure with the various points labeled according to Cohen's notation.[8] This figure can be considered as a distorted version of the truncated octahedral zone for a face-centered-cubic lattice, where the distortion consists of stretching along [111]. In the zone there are three distinct types of faces: viz., {111}, {100}, and {110} types whose centers are labeled T, L, and X in Fig. 1. The {100} faces are the largest and closest to the zone center Γ. The hexagonal-shaped {111} faces and the rectangular {110} faces are almost exactly the same distance from Γ; the former are only $\frac{1}{2}\%$ farther from the zone center than the latter.

Although directions in the rhombohedral system are not generally normal to planes bearing the same indices, there are the following exceptions: viz., $\langle 111 \rangle$, $\langle 1\bar{1}0 \rangle$, and $\langle 11\bar{2} \rangle$. All three $\langle 1\bar{1}0 \rangle$ and $\langle 11\bar{2} \rangle$ directions lie in the (111) plane. The [1$\bar{1}$0] direction is parallel to the line joining T and W, so that the (1$\bar{1}$0) plane bisects the Brillouin zone along a line X-U-T-U-L. This plane and its two other equivalents are the mirror planes in this system. The [1$\bar{1}$0] direction is one of the 3 twofold rotation axes, [11$\bar{2}$] is parallel to the line joining T and U, while [111] is parallel to the line Γ-T. Two other directions are of interest, viz., the direction parallel to U-X which is [001], and the direction parallel to L-U

which is [110]. Some additional data on the mercury Brillouin zone appear in Table I.

The most direct way of obtaining the free-electron model for the Fermi surface is by means of the geometrical construction of Harrison.[9] The Fermi radius of $0.652(2\pi/a_0) = 1.37$ Å^{-1} is more than sufficient to assure overlap into the second zone on the {100} faces but it is only equal to 95% of either the dimension Γ-X or Γ-T. This overlap is shown in Fig. 2, which illustrates the Brillouin zone with its inscribed Fermi sphere. Here the faces are labeled according to Jones'[10] notation; the (111) plane remains a T face, but the (100) and (110) faces are named A and B, respectively. The section of the Fermi sphere which cuts through the A face, along with that section from the adjoining zone, produces double-convex lens-shaped surfaces on each of the six equivalent {100} faces. Since the volume contained within each of these lenses is common to two of the Fermi spheres, the surfaces belong to the second Brillouin zone. These electron surfaces support elliptical orbits which we have called α orbits; they will have a minimum area of 0.44 Å^{-2} when the magnetic field lies in a (100) plane and a maximum area equal to 1.8 Å^{-2} when the field is perpendicular to a (100) plane.

From the dimensions in Table I, it is clear that the Fermi sphere does not touch either the faces B or T. The first-zone hole surface supports closed orbits with the field in two directions, viz., perpendicular to (100) and (11$\bar{2}$). The first of these, a section S-S of which is shown in Fig. 2, is a bow-tie across the shorter dimension of the (110) face. This orbit remains closed as a function of field direction within a considerable angular region of [100]. The other closed orbit on the hole surface is bone-shaped and lies in a (1$\bar{1}$0) plane about T. This orbit, which extends across the whole of the (111) face of the Brillouin zone, has area of 0.57 Å^{-2} in the (1$\bar{1}$0) plane. It becomes open as the field, and hence the normal to the plane of the orbit, is rotated towards [11$\bar{2}$]. In addition to these closed orbits, the hole surface supports open orbits to the (11$\bar{2}$), (1$\bar{1}$0), and (100) planes.

In the discussion of the experimental results which follows, it will be necessary to refer to crystallographic directions corresponding to the direction of the magnetic field or the axis of the crystal perpendicular to the plane of rotation of the magnetic field. In most cases it is possible to use the conventional notation, where the crystallographic indices enclosed in square brackets, i.e., [ ] or $\langle$ $\rangle$, indicate a direction or set of equivalent directions, respectively. However the directions in real space perpendicular to the (100) and (110) faces do not have small integral indices. In these cases, it is necessary to depart from the convention and use the plane indices with parentheses. Thus a crystal suspension with "the

[7] C. S. Barrett, Acta. Cryst. 10, 58 (1957).

[8] M. H. Cohen, Phys. Rev. 121, 387 (1961).

[9] W. A. Harrison, Phys. Rev. 118, 1182 (1960); 118, 1190 (1960).

[10] H. Jones, Theory of Brillouin Zones and Electronic Structure (Interscience Publishers, Inc., New York, 1960).

(100) vertical" means that the normal to the (100) plane is vertical and the plane itself is horizontal.

III. EXPERIMENT

a. Torque-Balance Apparatus

Much of the data below 30 kG was taken with an automatic torsion balance using a modified Weston "Inductronic Amplifier."[3] Magnetic fields in this range were produced by a Varian Model V3603 electromagnet, which was energized by a VFR 2501 field-regulated power supply. A retransmitting circuit in the supply provided a dc voltage proportional to the magnetic field; this voltage was used to drive the X axis of a Moseley 202A X-Y recorder. The dc output of the inductronic amplifier was fed to the Y axis of the recorder. When it was necessary to enhance higher frequency oscillations or to suppress a slowly varying field-dependent background signal, the output was time differentiated by an operational amplifier.

b. Rf Apparatus

Figure 3 shows a block diagram of the electronics used in the rf experiments. The modulation frequency in this apparatus is 35 kc/sec and the detection frequency is 70 kc/sec. A modulation field of about 10 to 15 G is produced by the 200 mW output of a Hewlett-Packard Model 200 CD oscillator. The 70-kc/sec reference signal for the Princeton Applied Research Model JB5 lock-in-amplifier is generated by a transistor frequency-doubling, limiting amplifier. This limiter assures that the amplitude of the reference signal is roughly independent of the modulation level.

The signal from the pickup coil, after traversing a bucking circuit to reduce the amplitude of the fundamental, is coupled to the Princeton Applied Research Model CR4 preamplifier through two filters and a matching transformer. A ferrite core transformer matches the high input impedance of the preamplifier, about 10 000 to 100 000 Ω, to the low impedance of the pickup coil, about 300 Ω. A bridged-tee 35-kc/sec rejection filter on the low-impedance side of the transformer and a 70-kc/sec bandpass filter on the high-impedance side reduce the amplitudes of unwanted signals. Further reduction in both the fundamental and the second-harmonic component produced by distortion in the oscillator output is effected by an astatic winding of the pick-up coil. This coil is wound in two sections, each of which contains 350 turns and fits inside a 400-turn modulation coil. Stray noise limits the over-all system gain to about 10^5. For strong signals the system was operated at a gain of about 10^4.

Part of the data using the rf method was taken below 30 kG, with the Varian magnet and a Dewar identical to that employed for the torque-balance experiments. Data taken at high fields between 50 and 60 kG required the use of a Westinghouse 55-kG super-
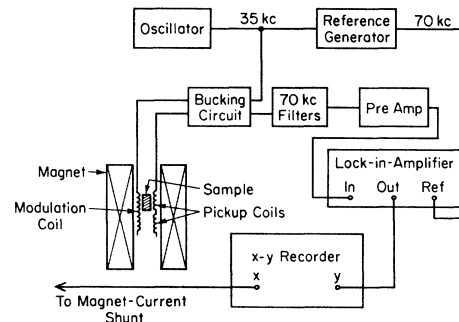

FIG. 3. Schematic arrangement of the electronics used in the rf technique.

conducting magnet. A conventional double-Dewar system, where the outer Dewar provides the nitrogen shielding for the inner helium Dewar, surrounds the magnet. The probe and sample are contained within a third inner helium Dewar, which tapers at the bottom to a 1-in.-diam access hole in the solenoid. By pumping on the innermost Dewar with a Hereaus 140-m³-per-hour pump, the sample temperature can be lowered to about 1.15°K. In this way, the superconducting magnet remains at 4.2°K and its high-field performance is unaffected by lowering the temperature of the experiment. The magnet is energized by a Westinghouse "Scamp" magnet control. Three 50-mV, 20-A, 1% meter shunts connected in series provide the drive for the X axis of the X-Y recorder. During each run the X axis of the recorder is calibrated by measuring the voltage across one of the shunts with a Rubicon potentiometer. A motor-driven helipot, connected to the control circuit of the magnet control, sweeps the field at about 1 kG/min. During an experiment, separate helium transfers are made into the magnet and sample Dewar after precooling the magnet with liquid nitrogen.

Two probes were constructed for use with the rf method, one for use with the conventional electromagnet, and one for use in the superconducting solenoid. Both probes fit vertically in their respective Dewars; the principal difference between them is that the probe for the conventional magnet holds the coil and sample assembly in a fixed orientation perpendicular to the axis of the probe and the field is rotated by rotating the magnet. The probe for the superconducting solenoid provides for rotation of the sample plus coils about a horizontal axis with respect to the fixed vertical field of the solenoid. Rotation of the sample is accomplished by means of a worm and gear drive mechanism similar to that described by Thorsen and Berlincourt.[11] The angle of the sample with respect to the field is indicated on a ten-turn dial at the top of the probe. This dial was calibrated by measuring optically, as a function of dial reading, the angle of a mirror attached in place of the sample.

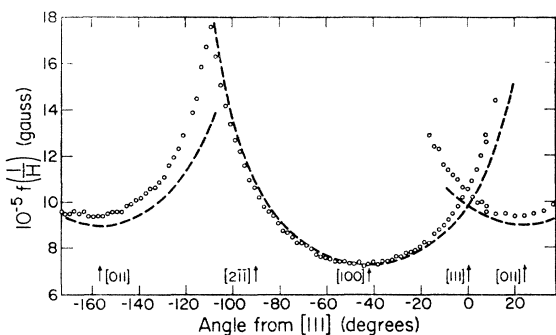[11] A. C. Thorsen and T. G. Berlincourt, Rev. Sci. Instr. 34, 435 (1963).

FIG. 4. Frequency $f(1/H)$ of dHvA oscillations with the magnetic field in (011) as a function of angle from [111]. These data were obtained with the torque balance between 19 and 29 kG. The dashed curves represent the expected behavior of cylinders along ⟨100⟩.

c. Magnetic-Field Calibration

Apart from errors in orientation of the sample and errors in interpretation of the final data, the only other errors in the dHvA measurements arise from measurements of the magnetic field. Errors in interpretation in principle at least should be negligible.

In the experiments performed using the conventional electromagnet, the field interval on the X-Y recorder was calibrated at the beginning and end of each day with a Rawson rotating-coil gaussmeter. It was found that after an initial warmup period of about half an hour, the field regulation of the power supply did not drift appreciably during a day's run The maximum drift observed over a 10-h period was 50 G at 25 kG, a total change of about 0.2%. The stated accuracy of the Rawson meter is given as 0.1% on all ranges. This was calibrated over a field range from 2 kG to about 19 kG by observing the proton Li^7 and deuteron magnetic resonances at frequencies measured with a Hewlett Packard Model 524 L frequency counter. The accuracy of the Rawson meter on all of its ranges was found to be well within the limits claimed by the manufacturer.

The calibration of the superconducting magnet presents a somewhat more difficult technical problem. It is known that because of flux trapping in the windings of the magnet, superconducting magnets exhibit hysteresis effects at high fields amounting to as much as 1% of the operating field.[12,13] Any attempt to calibrate the field as a function of current to an accuracy better than 1% thus would be futile. Since there is no convenient way of measuring the magnetic field at the sample during the course of the experiment, the manufacturer's coil constant was used in this work. To check the accuracy of this procedure, dHvA frequencies in mercury were measured in orientations for which rf data had been obtained in the calibrated Varian magnet. The frequencies taken in several directions, where their value

was insensitive to orientation, agreed with the low-field data within the over-all 2% accuracy of the experiments. During an experiment care was taken to avoid inductive effects in the magnet by counting the number of oscillations between *static* values of the field.

d. Sample Preparation

When cooled carefully from room temperature, mercury forms large single crystals at −38.8°C, changing from its normally silvery appearance as a liquid to a faintly bluish cast as a solid. The crystals are soft even when cooled to liquid-nitrogen temperature and are damaged and deformed easily.

All the samples for the torque-balance experiments and one used in the rf experiment were prepared from "instrument grade" mercury[14] with stated impurities of less than 0.0006%. The remaining specimens used in the rf experiment were prepared from 99.99999% pure mercury from a separate source[15]; no differences in the dHvA effect were observed between the two purities. The two types of apparatus used in the torque balance and the rf techniques dictate different sample geometries. The former allows large samples of irregular shape which can be rotated to the appropriate orientation, whereas the latter requires small (3 mm by 4 mm) cylinders with the desired *plane* of rotation passing through the cylinder axis. For both types of experiments the single-crystal samples were grown by a modified Bridgman technique, in which the mercury was slowly cooled in beeswax or C-8 epoxy molds. The orientation was determined by back-reflection Laue pictures taken on the as-grown crystal surfaces at liquid-nitrogen temperature. In neither set of experiments was there any attempt to obtain seeded crystals. For the torque balance, the crystal was attached to a copper wire, which
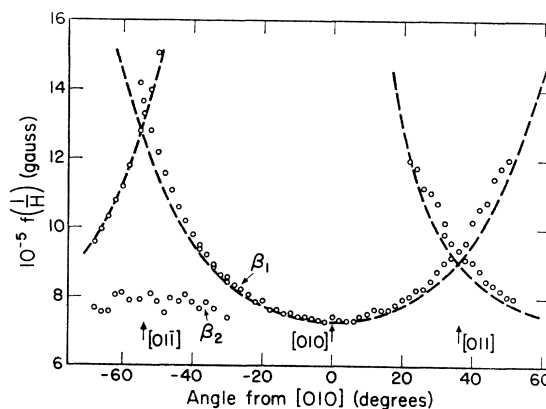

FIG. 5. Low-field torque-balance data obtained with the magnetic field in the (100) plane. The dashed curves represent the expected behavior of cylinders along ⟨100⟩.

[12] M. S. Lubell (private communication).
[13] B. W. Maxfield and J. R. Merrill, Rev. Sci. Instr. **36**, 1083 (1965).
[14] Fisher Scientific Company, Pittsburgh, Pennsylvania, Catalog # M-141.
[15] United Mineral & Chemical Corporation, 16 Hudson Street New York 13, New York.

was bent so that the desired direction was vertical. By judicious selection of samples for the rf method, it was found possible to obtain a specimen with the desired crystal plane passing through the cylinder axis.

IV. RESULTS

a. Low-Field Torque-Balance Data

Figure 4 shows a plot of data taken with the torque balance over a field interval from 19 to 29 kG, at a temperature of 1.15°K. In this illustration are plotted the observed frequencies $f(1/H)$ of the dHvA oscillations as a function of the angle of the field from the [111] direction. The frequency and the area are related by Eq. (2). The dominant feature of this traverse with the field in a (01$\bar{1}$) plane is the frequency which increases roughly as $1/\cos\theta$, here θ is the angle H makes with [100]. This functional behavior would result from cylindrical portions of the Fermi surface with their axes aligned along ⟨100⟩. In Figs. 4 through 7, the dashed curves represent the angular behavior expected from such cylinders, where the minimum cross sections are normalized to the minimum value observed. The three-plane-wave (3PW) model, to be discussed below, predicts an angular variation for these portions of the FS which is very close to the predictions of this "cylinder model." Reference to Fig. 4 shows that a second frequency appears near [111], decreases to a minimum along [011], increases rapidly toward [2$\bar{1}\bar{1}$], and then disappears in the same vicinity as the first frequency. These frequencies are characteristic of all the low-field data taken with the torque balance and correspond to the small, highly anisotropic portions of the FS first observed by Verkin et al.[1] and Shoenberg.[2]

Figure 5 illustrates a traverse with the field lying in a (100) plane; again the frequencies exhibit a cylindrical behavior, increasing rapidly away from [010]. Note that in this case, [011] is a crossing point rather than a

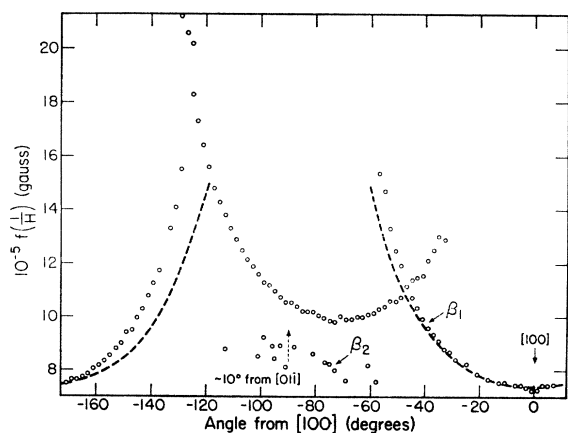Fig. 6. Low-field torque balance data obtained with the magnetic field in plane tilted about 10° relative to a (011) plane; the resulting asymmetry of the data is clearly visible. The dashed curves represent the expected behavior of cylindres along ⟨100⟩.
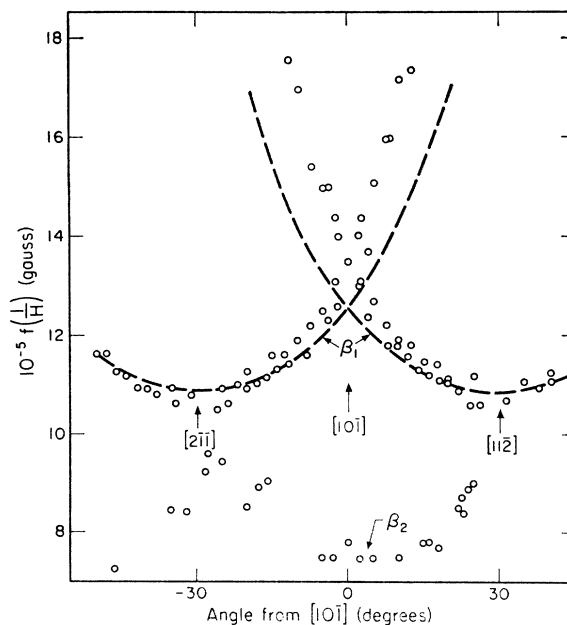

Fig. 7. Low-field torque-balance data obtained with the magnetic field in the (111) basal plane. The dashed curves represent the expected behavior of cylinders along ⟨100⟩.

minimum as in the previous example. In both cases, the areas of these features increase markedly as one approaches the [01$\bar{1}$] and [2$\bar{1}\bar{1}$] directions, which lie in the (111) plane. Although it is not indicated in the illustrations, the amplitude of the oscillations decreases as H approaches the basal plane, (111), indicating that the "quality" of the extremum of the orbits is deteriorating. A possible explanation is that in this region orbits, differing by small angles from the dominant one, become open and hence carriers traversing them are lost and do not contribute to the signal. Figure 6 shows another traverse, this time with the field in a (011) plane. This crystal was misoriented by about 10° and hence there is a minimum 30° from [01$\bar{1}$] rather than a crossing point; again one of the areas comes to a minimum along [100]. Finally consider Fig. 7, a plot of the traverse with H lying in the (111) plane. Here the dominant oscillations increase from a minimum of about 10.6×10^5 G along [11$\bar{2}$] to a crossing point at [10$\bar{1}$] of about 13.5×10^5 G.

These data, as has been reported earlier,[16] can be assigned to tubular portions of the Fermi surface extending in length along ⟨100⟩ directions with minimum areas for H parallel to ⟨100⟩. Rather than pinching off, as would cigar-shaped surfaces, these sections increase in area along the line K-W from their minimum in the vicinity of the point K. They connect with larger surfaces lying in the (111) planes in the vicinity of the point W. The minimum frequency observed (7.4×10^5 G) in the (011), (01$\bar{1}$) and (100) traverses corresponds to the minimum area of these tubes. The local mini-

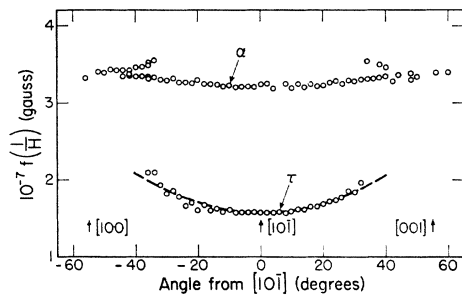[16] G. B. Brandt and J. A. Rayne, Phys. Letters **15**, 18 (1965).

Fig. 8. Low-field rf data obtained with the magnetic field in the (010) plane. The dashed curve in the lower part of the figure corresponds to the expected behavior from a cylinder oriented along [101].

mum of 9.4×10^5 G in Fig. 4 corresponds to an orbit associated with the other two {110} faces, which are inclined to the field at about 35°. In the (100) traverse of Fig. 5, the orbits associated with the {110} faces, which presented a minimum along [011] in the previous figure, are separated as the field is rotated from [011]; one increases and the other decreases as the field moves toward [010]. Because of the misorientation of the sample, only one of the two other β orbits is seen in Fig. 6 between [011] and [100]; the other orbit is so inclined as to be very large or open in this region. In Fig. 7, all three of the oblique β orbits repeat their minima every 60°, becoming open at 90° from each minimum.

As was discussed in the preliminary report of this work,[16] no features of the free-electron model correspond in area to the observed β oscillations. The bow-tie orbit across the (110) faces does exhibit the appropriate angular behavior; its minimum area, however, is an order of magnitude too large. In the three-parameter model to be described later, the bow-tie is split into two sections of the correct area, one on either side of the center of the (110) face.

In Fig. 5, 6, and 7, near [011], there are scattered points centering about a frequency of approximately 8×10^5 G. These points come from very poorly resolved beats in the dominant frequency and are seen only near this direction. They are not seen for **H** more than 20° out of the (111) plane. Areas with this behavior do not appear as a consequence of either the free-electron or the OPW models; the origin of these frequencies is thus somewhat of a mystery. Because of the poor resolution, it is difficult to do more than speculate about their origin. Perhaps a more detailed band structure calculation might produce small pieces of Fermi surface, possibly at U or W, which would explain these frequencies.

b. Low-Field Results Using the rf Technique

Low-field data taken with the rf technique reveal two distinct types of oscillations, one having a frequency roughly twice the other. Figure 8 shows the results for the field lying in the (010) plane. From the

angular behavior of the two sets of oscillations, it is clear that the higher frequency component is not simply the second harmonic of the lower; the latter frequency varies as $1/\cos\theta$, where θ is the angle from [101], while the former is roughly isotropic in this plot. The higher frequency oscillations are associated with orbits on the lens-shaped portions of the Fermi surface and are referred to as α oscillations. For reasons which will become clear in the discussion of the three-parameter plane-wave model, the other oscillations are referred to as τ oscillations.

In Fig. 9 the data for **H** in the (111) plane are plotted. It should be noted that in this and the previous figure, the vertical scale is in units of 10^7 G rather than 10^5 G as in the plots of the β oscillations. Thus the dominant areas observed with the rf method are over an order of magnitude larger than those observed with the torque balance at the same field. This demonstrates clearly the sensitivity of the rf method to dHvA frequencies, whose field intervals per oscillation (about 46 and 23 G for the τ and α oscillations, respectively) are on the same order of magnitude as the modulating field (about 15 G peak to peak). The corresponding field interval for the β oscillations is about 400 G at these fields, and although they are observable in some of the data, their presence here has been virtually eliminated by time differentiation of the receiver output. A noticeable feature of Fig. 9 is the peculiar abrupt variation of the τ oscillations about 15° from [101]. The oscillations actually disappear for about 2° in these regions and the change from the lower to the higher frequency is discontinuous, with no observed intermediate value. This behavior, which is reproduced by the predictions of the plane-wave model, occurs when the plane of the orbit intersects one of the tubular sections of the Fermi surface lying along ⟨100⟩ directions. When the τ orbits pass over the intersection of these tubes with the surface on the {111} planes, they become open for a small angular range.
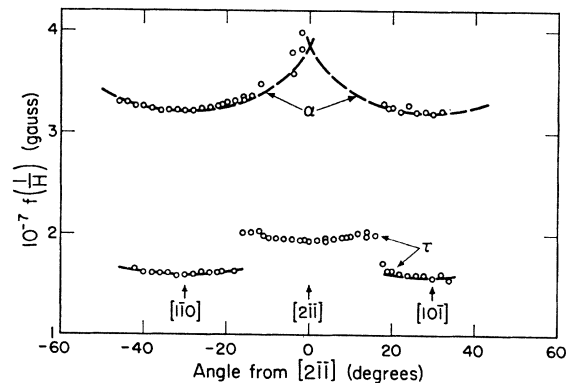

Fig. 9. Low-field rf data obtained with the magnetic field in the (111) basal plane. The dashed curves in the upper part of the figure correspond to the expected behavior of ellipsoidal discs on the {100} zone faces.

The α oscillations, shown in Figs. 8 and 9, are the only feature whose behavior is predicted even qualitatively by the free-electron model. These oscillations arise from orbits on the disc-shaped surfaces lying in the {100} planes; in this field range these discs are observed edge-on only. Although the observed areas are only 75% of the free-electron predictions, in all directions their angular behavior is exactly the same as both the free-electron and the 3PW predictions. The dashed curve in Fig. 9 represents the angular variation of the area of an ellipsoid with minimum area equal to the minimum observed for the α oscillations.

Up to this point the origin of the τ oscillations has been left somewhat of a mystery. Like the β oscillations, the τ oscillations do not fit any features of the free-electron model. To explain their origin, it is necessary to allow orbits with centers roughly at U to pass through the (111) planes in the vicinity of T and through (100) plane in the vicinity of X. The situation here is completely analogous to the problem in explaining the β orbits, viz., in order to produce FS areas of the appropriate size and angular behavior, the first and second bands must be split so that the Fermi energy lies in the band gap at the points T and X. Fortunately, this requirement is produced by the plane-wave model discussed later.

c. High-Field Measurements

In the hope of increasing the information concerning the angular variation of the α oscillations, and particularly in the hope of determining the value of the maximum area of the lenses, the rf measurements were extended to 60 kG by the use of the superconducting solenoid system described earlier. The data obtained between 52 and 60 kG, with H lying in (01$\bar{1}$) and H lying in a plane perpendicular to the [001] direction, are shown in Figs. 10 and 11. These traverses were both on the same sample, in which the crystal axis was oriented within 2° of (100). Frequencies on the order of 6.8×10^7 G were observed for H in the immediate vicinity of (100). These frequencies appear to result from the maximum cross section of the lenses; it should be noted that there is a break in the frequency scale
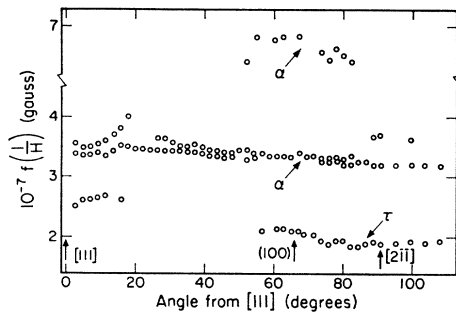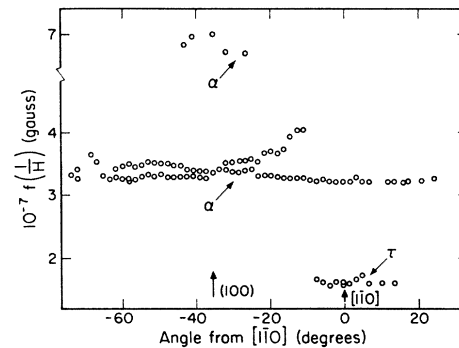

FIG. 11. High-field rf data taken with the magnetic field lying in a plane normal to [001]. These results were obtained on the same sample used for the experiments corresponding to the previous figure.

at 4.0×10^7. Because of their weak intensity, the high-frequency oscillations with H parallel to (100) were difficult to observe, thus accounting for the large amount of scatter in these data. As in the case of the α oscillations, the possibility of these being harmonics of lower frequencies is ruled out by the change in phase of the high-frequency oscillations relative to the lower ones. The poorly defined oscillations of frequency about 2.6×10^7 G in the vicinity of [111] are probably associated in some way with the surfaces producing the τ oscillations. No more definite interpretation presents itself, since they are unexplainable in terms of either the free-electron or plane-wave models.

d. Effective-Mass Measurements

The effective mass of the β oscillations was determined, as a function of angle, from the temperature variation of the amplitude of the torque oscillations between 1.1 and 4.2°K for (011), (01$\bar{1}$), and (100) traverses. Figure 12 shows the results for one traverse; the effective mass varies from a minimum of about $0.12m_0$ to as high as $0.25m_0$. There seems to be a rough correlation between increasing m^*/m_0 and increasing orbit area, as one expects from consideration of the free-electron model.

Measurements were made of the amplitude of the torque as a function of field in the vicinity of [100] in order to estimate the value of T^*, the effective scattering temperature. Measurements at 4.2°K gave a value of 0.3°K and measurements at 1.2°K gave a value of 2.0°K. In the few cases where the value of this parameter has been determined, its value usually has been found to be about 1°K. The large temperature dependence of T^* is most unexpected and is thought to be due to the large electron-phonon interaction effects in mercury.[17]

The effective mass m^*/m_0 of the τ oscillations, in two separate but equivalent temperature runs, was found to lie between 0.9 and 1.1 with H parallel to

FIG. 10. Rf data obtained with a magnetic field between 52 and 60 kG lying in the (01$\bar{1}$) plane. Note the break in the frequency scale.

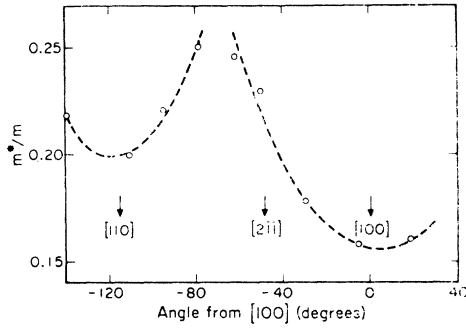[17] A. B. Pippard (private communication).

FIG. 12. Effective mass of the β oscillations a as function of angle in the $(01\bar{1})$ plane. (*Note added in proof.* The direction designated as [110] should read [011].)

[101]. No detailed angular study was possible in this case because the rf amplitude decreased quite rapidly with temperature. An attempt to determine the effective mass of the minimum area of the α oscillations failed because the oscillations were observed only at the very lowest temperature range of the system. From the rate at which these oscillations disappeared with increase in temperature, it was clear that the effective masses of the associated orbits are somewhat higher than those of the τ oscillations.

e. Summary of the dHvA Data

The data obtained by the two techniques over the field range 10 to 60 kG indicate three general features of the Fermi surface responsible for the three types of orbits observed. Two sets of oscillations can be associated with the first-zone hole surface, and the third, the α oscillations, are associated with the lens-shaped second-zone electron surfaces predicted by both the free-electron and plane-wave models. The data are all consistent with the general topology of the free-electron model, providing modifications are made at the points T and X in the Brillouin zone. The effective masses, measured for the two orbits associated with the hole surface, are of the same order of magnitude as those predicted by the three PW model. The data are summarized in Table II along with the predictions of both the free-electron model and the predictions of the plane-wave model discussed below.

V. PLANE-WAVE FITTING PROCEDURE

As Harrison has discussed at some length,[9,18,19] the Fermi surfaces of a number of metals can be calculated to a surprising degree of accuracy in the nearly-free-electron approximation, where the deviations from free-electron behavior can be expressed in terms of matrix elements between plane-wave states of an effective pseudopotential.[20,21] The advantage of this for-

[18] W. A. Harrison, Phys. Rev. **131**, 2433 (1963).
[19] W. A. Harrison, Phys. Rev. **129**, 2503 (1963); **129**, 2512 (1963).
[20] J. C. Phillips and L. Kleinman, Phys. Rev. **116**, 287 (1959).
[21] J. M. Ziman, Advan. Phys. **13**, 89 (1964).

TABLE II. Experimental data compared with free-electron and three PW models.

Direction of H	Type of orbit	$10^{-6} f(1/H)$ (gauss)	Area (Å^{-2}) Experimental	3 PW	Free electron	m^*/m_0
			[01$\bar{1}$] vertical			
[011]	β	9.4	0.0089	0.0094	0.111	0.20
	α	340	0.324	0.366	0.441	...
[2$\bar{1}\bar{1}$]	β	10.6	0.0101	0.0105	0.175	0.23
	τ	190	0.1810	0.151	0.570	...
	α	320	0.305	0.397	0.510	...
	α	370	0.354	0.402	0.490	...
(100)	β	8.15	0.0078	0.0078	0.119	0.17
	τ	215	0.206	0.166	open	...
	α	334	0.320	0.359	0.454	...
	α	680	0.650	1.19	1.80	...
[100]	β	7.35	0.0070	0.0070	0.098	0.16(0.07ᵃ)
	α	340	0.324	0.352	0.441	...
[111]	β	10.6	0.0101	0.0094	0.121	...
	α	345	0.330	0.400	0.480	...
	?	260	0.248	...	...	...
			(010) vertical			
[10$\bar{1}$]	β	13.3	0.0127	0.0126	open	0.15
	τ	158	0.151	0.107	open	0.90(0.40ᵃ)
	α	322	0.305	0.344	0.441	...
	?	8.0	0.0077	...	...	...
[001]	β	7.35	0.0070	0.0070	0.098	0.16(0.07ᵃ)
	α	340	0.324	0.352	0.441	...
[101]	β	9.4	0.0089	0.0090	0.111	0.20
			(110) vertical			
	β	10.8ᵇ	0.0103ᵇ	0.0126	open	0.15
[1$\bar{1}$0]	τ	158	0.151	0.107	open	0.90(0.40ᵃ)
	α	322	0.308	0.344	0.441	...
[001]	β	7.35	0.0070	0.0070	0.098	0.16(0.07ᵃ)
			[111] vertical			
[10$\bar{1}$]	β	13.5	0.0129	0.0130	open	0.15
	τ	158	0.151	0.107	open	0.90(0.40ᵃ)
	α	320	0.308	0.344	0.441	...
	?	7.5	0.0072	...	...	...
[2$\bar{1}\bar{1}$]	β	10.8	0.0103	0.0104	0.175	0.23
	τ	195	0.186	0.151	0.570	...
	α	400	0.381	0.397	0.510	...
			[001] vertical			
[1$\bar{1}$0]	β	13.5	0.0129	0.0130	open	0.15
	τ	158	0.151	0.107	open	0.90(0.40ᵃ)
	α	322	0.308	0.344	0.441	...
(100)	α	334	0.320	0.359	0.454	...
	τ	220	0.210	0.166	open	...
(110)	α	335	0.322	0.390	0.470	...
	τ	200	0.191	0.204	open	...

ᵃ Calculated from the 3 PW model.
ᵇ Sample misoriented by 10 deg.

malism is that the perturbing potential, the sum of the crystal potential and the repulsive potential resulting from orthogonalizing plane waves to the core wave functions, is small and can be expanded in terms of a Fourier series of a few reciprocal lattice vectors. Thus we can write

$$V_{\text{pseudo}} = \sum_{\mathbf{K}_j} V_{\mathbf{K}_j} \exp i\mathbf{K}_j \cdot \mathbf{r}, \qquad (7)$$

where the Fourier components $V_{\mathbf{K}_j}$ rapidly decrease in magnitude with increasing magnitude of the reciprocal lattice vector $\mathbf{K}_j$.

The Hamiltonian, in terms of that for a free electron, is

$$H = H_0 + V_{\text{pseudo}} = H_0 + \sum_{\mathbf{K}_j} V_{\mathbf{K}_j} \exp i\mathbf{K}_j \cdot \mathbf{r}. \qquad (8)$$

To determine the energy bands as a function of wave vector $\mathbf{k}$, it is necessary to diagonalize the matrix of H. In the representation where the states $\langle l|$ and $|m\rangle$ are plane waves of the form $\exp[-i(\mathbf{k}+\mathbf{K}_l)\cdot\mathbf{r}]$ and $\exp[i(\mathbf{k}+\mathbf{K}_m)\cdot\mathbf{r}]$ respectively, the matrix is

$$\langle l|H|m\rangle = \begin{pmatrix} (\hbar^2/2m)(\mathbf{k}+\mathbf{K}_1)^2 & V_{\mathbf{K}_1-\mathbf{K}_2} & V_{\mathbf{K}_1-\mathbf{K}_3} & \cdots \\ V_{\mathbf{K}_2-\mathbf{K}_1} & (\hbar^2/2m)(\mathbf{k}+\mathbf{K}_2)^2 & V_{\mathbf{K}_2-\mathbf{K}_3} & \cdots \\ V_{\mathbf{K}_3-\mathbf{K}_1} & V_{\mathbf{K}_3-\mathbf{K}_2} & (\hbar^2/2m)(\mathbf{k}+\mathbf{K}_3)^2 & \cdots \\ \vdots & \vdots & \vdots \end{pmatrix}, \quad (9)$$

where the diagonal terms of the pseudopotential V_{000} have been set equal to zero. The remaining diagonal terms are just the energy, quadratic in wave vector, which is obtained from the free-electron case. In this representation the off-diagonal terms involve only the pseudopotential and are of the form

$$\langle l|V_{\text{pseudo}}|m\rangle = \int d\mathbf{r} \exp[-i(\mathbf{K}_l\cdot\mathbf{r}-\mathbf{K}_m\cdot\mathbf{r})]\sum_{\mathbf{K}_j} V_{\mathbf{K}_j}$$

$$\times \exp i\mathbf{K}_j\cdot\mathbf{r}. \quad (10)$$

In Eq. (10) the terms in the integral corresponding to the various $\mathbf{K}_j$ will be oscillatory and the integral over the crystal will vanish unless $\mathbf{K}_j - (\mathbf{K}_l - \mathbf{K}_m) = 0$. In this case, the integral is equal to $V_{\mathbf{K}_j}$ or equivalently, $V_{\mathbf{K}_l-\mathbf{K}_m}$, the Fourier component of the potential corresponding to the reciprocal lattice vector $\mathbf{K}_j = \mathbf{K}_l - \mathbf{K}_m$. Although this treatment has considered the $V_{\mathbf{K}_j}$ as discrete variables associated with only those $\mathbf{k}$ vectors which are reciprocal lattice vectors, it is clear that the value of $V_{\mathbf{K}_j}$ must be equal to the value taken on by the continuous Fourier transform $V(\mathbf{k})$ of the spherically symmetric potential at $\mathbf{k} = \mathbf{K}_j$. Because the pseudopotential and its transform are continuous, it follows that $V_{\mathbf{K}_i} = V_{\mathbf{K}_j}$ if $\mathbf{K}_i = \mathbf{K}_j$. Ziman[21,22] has discussed at length the properties of the pseudopotential and its Fourier transform, and shows examples for several metals in his review article.

Although the pseudopotential can be calculated from knowledge of the free-ion potential and wave functions, this formalism can be inverted and the pseudopotential parameters can be regarded as adjustable parameters in fitting a model of the Fermi surface to the observed data on the Fermi surface.[23–25] A fitting program based on these considerations was used to produce a model of the mercury Fermi surface which fits, qualitatively, the experimental results discussed in Sec. IV. It was decided to limit the number of parameters to three and to consider only pseudopotential elements associated with the planes bounding the first Brillouin zone. Of these three parameters, V_{100}, V_{110}, and V_{111}, the latter two are nearly equal since the (110) and (111) reciprocal

Table III. Values of the pseudopotential coefficient energies in rydbergs.

	V_{100}	V_{110}	V_{111}
This work	−0.066	0.047	0.047
Theoretical[a]	−0.028	0.053	0.053

[a] See Ref. 27.

lattice vectors differ in length by only $\frac{1}{2}\%$.[26] Thus only two parameters associated with the three wave vectors remain to be varied, since the Fermi energy was not considered a parameter and was kept at its free-electron value. Eigenvalues of the resulting matrix were determined as a function of $\mathbf{k}$ on an IBM 7040 computer; owing to the restriction on $\mathbf{K}_i$, this matrix never exceeded 6×6. A binary search routine in the fitting program found that value of $\mathbf{k}$ in a given direction for which an eigenvalue equaled the Fermi energy. After the value of the $\mathbf{k}$ was recorded, the search proceeded along another nearby direction until the complete orbit was traced out.

During the course of the fitting procedure, certain restrictions on the sizes of the matrix elements, consistent with the topology required by the experimental data, were discovered. Values of V_{100} much less than -0.08 Ry and values of V_{110} and V_{111} less than $+0.03$ Ry do not produce a model with the thin tubular sections along $\langle 100 \rangle$. Figure 13 shows the effects on these tubular sections of varying the parameters V_{110} and V_{100} around their final values. From this illustra-
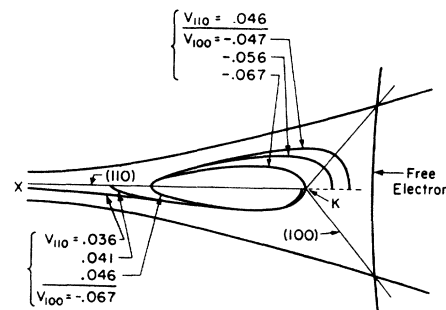

FIG. 13. Computed cross section of the first-zone hole surface, responsible for the β oscillations, as a function of the pseudopotential parameters V_{100}, V_{110}, and V_{111}.

[22] J. M. Ziman, *Principles of the Theory of Solids* (Cambridge University Press, Cambridge, England, 1964), pp. 94–97.

[23] J. R. Anderson and A. V. Gold, Phys. Rev. **139**, A1459 (1965).

[24] L. M. Falicov and Stuart Golin, Phys. Rev. **137**, A871 (1965).

[25] D. Brust, Phys. Rev. **134**, A1337 (1964).

[26] Note that the parameter $V_{\mathbf{K}_j}$ is a function only of the magnitude of the reciprocal lattice vector, since the potential is assumed to be spherically symmetric.
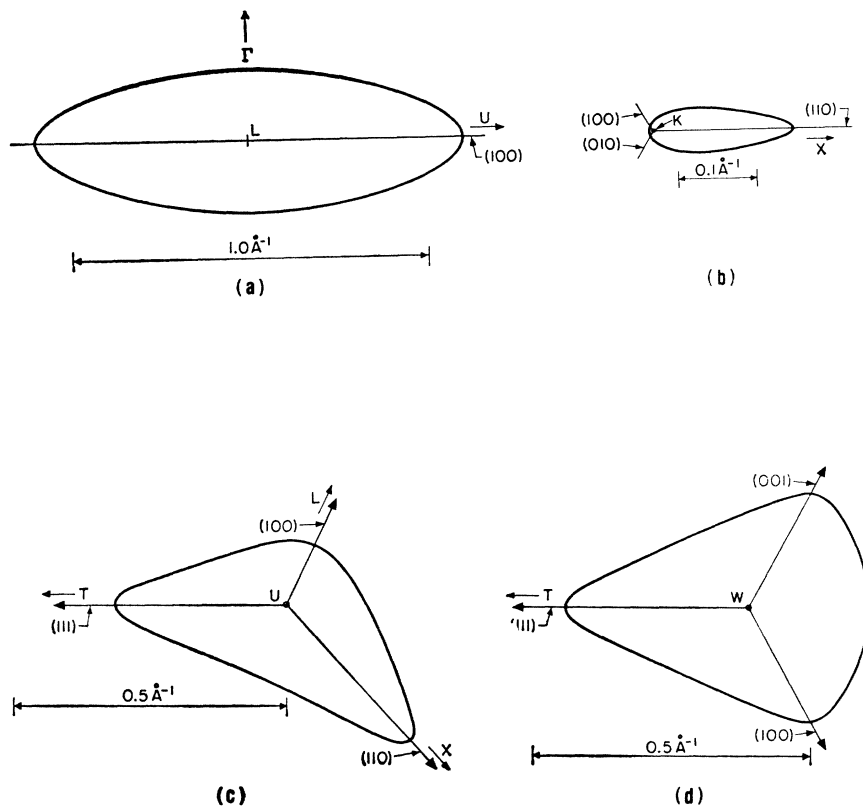
Fig. 14. Computed cross sections of the Fermi surface of mercury for the pseudopotential parameters given in Table III. The inset (a) refers to the second-zone discs, the inset (b) to that part of the hole surface responsible for the β oscillations and insets (c), (d) to that part of the hole surface responsible for the τ oscillations.

tion it is clear that the effect of making V_{100} more negative is to push the tubular section away from the zone edge at K. Making V_{110} more positive pushes the surface away from X towards K, while increasing the absolute magnitude of either parameter tends to decrease the area of the tubular section. Note that for one set of parameters a surface, which remains connected across the (110) face at X, is produced. This surface has the same topology as that of the free-electron model and is not consistent with the experiments. The final values of the parameters appear in Table III, where they are compared with corresponding values obtained from a semiempirical calculation of the pseudopotential.[27] Because the portion of the Fermi surface in the vicinity of K is the most sensitive to changes in the parameters, the minimum cross section of this feature was fitted to the β oscillations at the expense of the fit to the other two sets of oscillations. It is likely that a calculation involving 20 or 30 PW's would improve the quantitative agreement between the model and the α and τ oscillations. Figure 14 shows the cross sections of the calculated Fermi surface, while Fig. 15 illustrates the energy bands in the vicinity of the Fermi level. For comparison with these results, the free-electron energy bands are shown in Figs. 16 and 17. It should be emphasized that different numbers of plane waves

were employed in determining the eigenvalues along different symmetry directions. This results in discrepancies in the *higher energy levels* at certain symmetry points (c.f., point U in lower part of Fig. 15). For this reason only those levels near the Fermi energy should
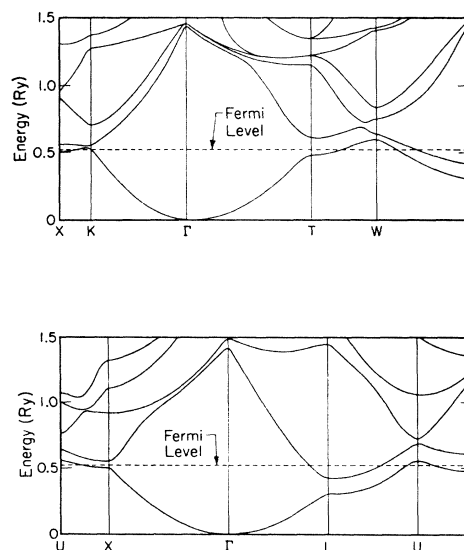

Fig. 15. Computed E-versus-k curves for mercury using the pseudopotential parameters of Table III.

[27] A. O. E. Animalu and V. Heine, Phil. Mag. **12**, 1249 (1965).

FIG. 16. Free-electron energy bands for mercury along the lines of symmetry U-X-Γ-L-U-T. The figures in parentheses are the relevant Miller indices for the plane waves; degeneracies for the higher states are also shown.
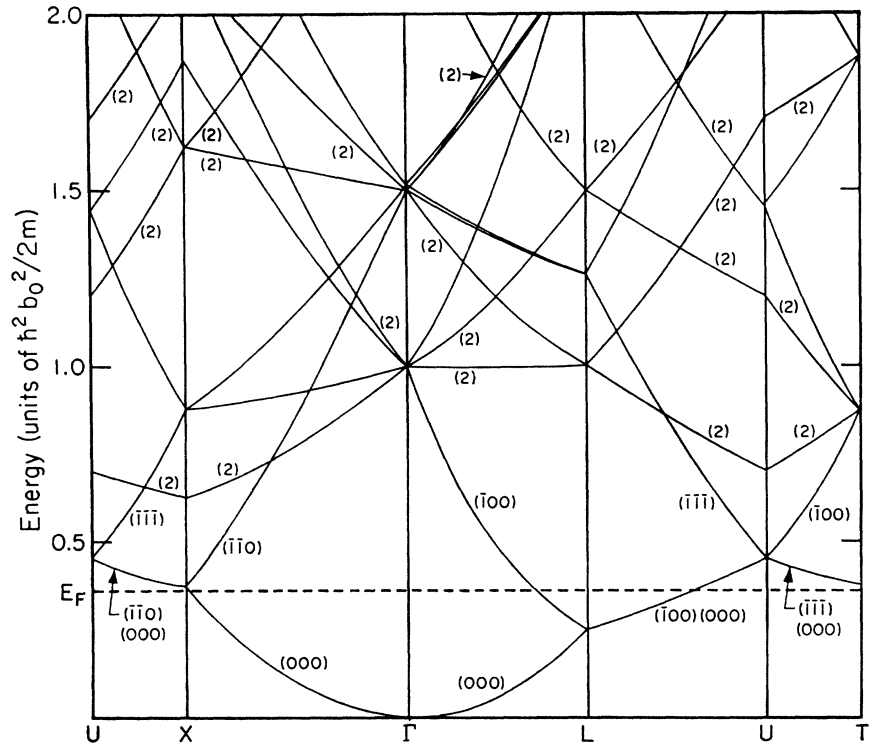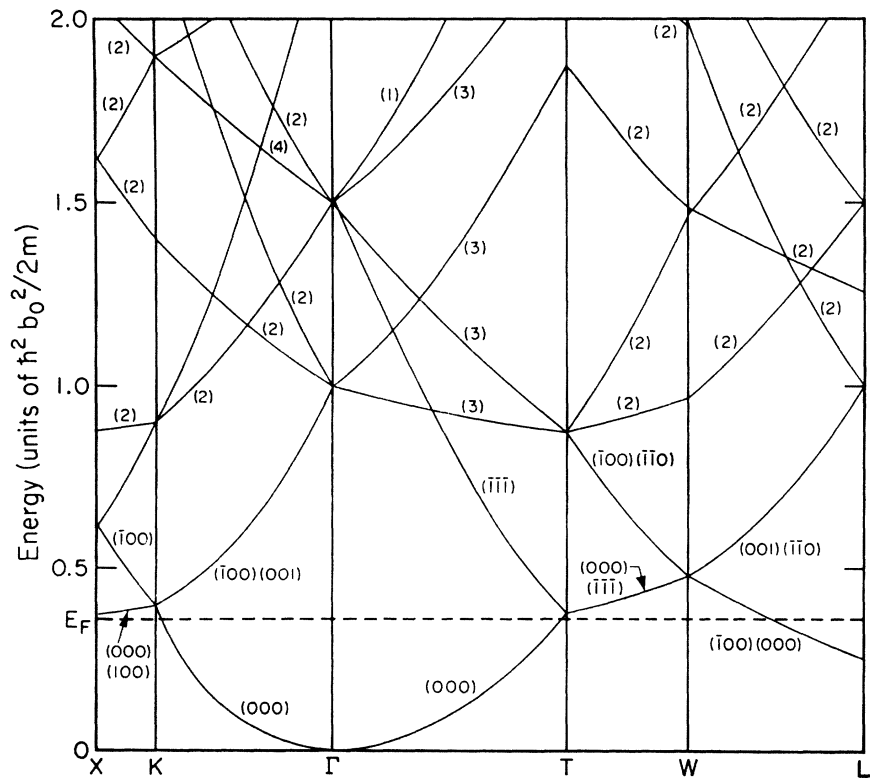

FIG. 17. Free-electron energy bands for mercury along the lines of symmetry X-K-Γ-T-W-L.

be regarded as being significant. A sketch of the first-zone Fermi surface resulting from the plane-wave fitting procedure is shown in Fig. 18.

Figure 19 shows the Fourier transform of a pseudopotential for mercury obtained from the calculation by Animalu and Heine.[27] For comparison, the points corresponding to the matrix elements V_{100} and V_{110} ($V_{110} = V_{111}$) are shown. Since these points were obtained by fitting the model of the Fermi surface to the experimental data without prior knowledge of the theoretical results, the agreement is reasonable. It should be pointed out, however, that the condition of change compensation ($n_e = n_h$) has not been maintained in our calculations. The error introduced by the neglect of this requirement may be quite serious and could in fact cause part of the discrepancy between the values of V_{100} given in Table I. Spin-orbit effects have not been *explicitly* considered in the present work. Since the crystal potential already lifts the degeneracy of the bands near the Fermi level, the fitting procedure automatically incorporates spin-orbit coupling into the matrix elements. Thus part of the above discrepancy could in fact be due to these effects. The situation is to be contrasted to that in lead[23] and arsenic,[24,28] where the band degeneracy is partly lifted by spin-orbit coupling. In this connection, it is of interest that
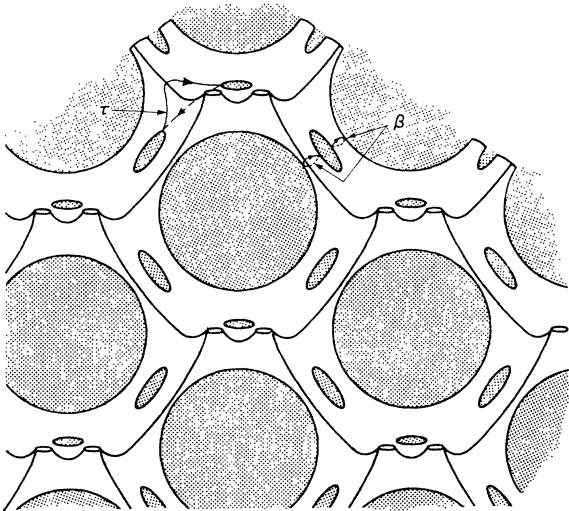

FIG. 18. Pictorial representation of computed first-zone hole surface for mercury in an extended zone scheme.
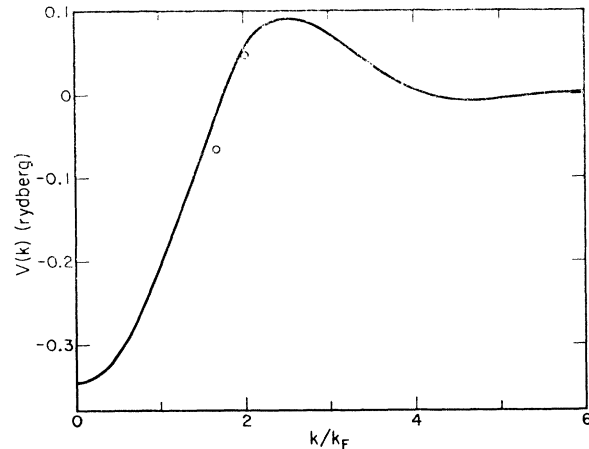
[28] Stuart Golin, Phys. Rev. **140**, A993 (1965).

FIG. 19. Pseudopotential for mercury computed by Animalu and Heine. The circles represent the values obtained by the fitting procedure in this work.

relativistic band calculations on mercury[29] indicate that the form of the Fermi surface is indeed close to that obtained by the present calculation.

VI. CONCLUSION

Studies of the de Haas–van Alphen effect in the field range from 10 to 60 kG validate a model of the Fermi surface, which is a recognizable distortion of the free-electron model. These distortions involve the reduction in area of the free-electron features and the alteration of the connectivity of the hole surface at the centers of the (110) and (111) faces of the Brillouin zone. A three-parameter plane-wave model fitted to the data reproduces the observed topology of the first-zone hole and the second-zone electron surfaces.

ACKNOWLEDGMENTS

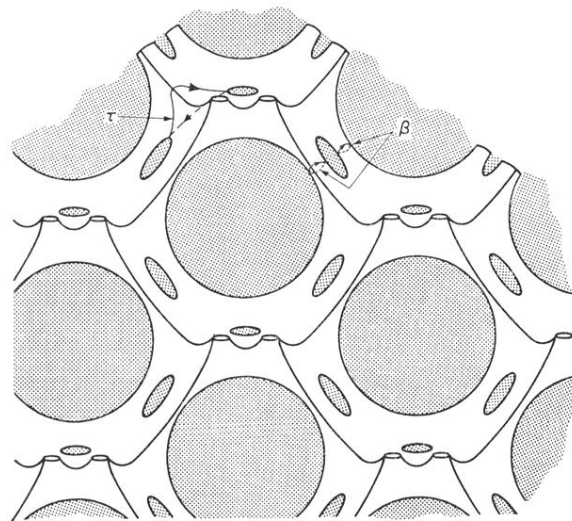[29] T. L. Loucks (to be published).

FIG. 18. Pictorial representation of computed first-zone hole surface for mercury in an extended zone scheme.